Design, Fabrication and Characterization of a Micro-Machined Gravity Gradiometer Suspension

Huafeng Liu, W.T. Pike and Guangbin Dou
Optical and Semiconductor Devices Group
Imperial College London
London, UK
w.t.pike@imperial.ac.uk

***Abstract*— This paper presents the design, fabrication and characterization of a suspension for rotational micromachined sensors with an ultra-low rotational spring stiffness but very high spurious-modes rejection ratios. This suspension is applied to a micro-machined gravity gradiometer for satellite gravity surveys, achieving a 3.38 Hz resonant frequency with the first spurious rejection ratio of 23.**

Keywords—Gravity Gradiometer; MEMS; Rotary Suspension

I. INTRODUCTION

Gravity gradiometers have been developed since the late 1890s for earth observations including exploration for minerals and hydrocarbons, underground structure and even the crustal anomaly and other valuable applications [1]. Generally, two principals are used for gravity gradiometry: torsion balance and differential accelerometers. The first working gravity gradiometer was invented by Loránd Eötvös on the basis of torsion balance and the gravity gradient unit is named as E (Eötvös) which is $10^{-9}/s^2$ or 10^{-4}mGal/m [2]. However, most commercial and space-grade gradiometers are based on differential accelerometers, such as Air-FTG [3], FALCON [4], GRACE [5] and GOCE [6]. Differential-accelerometer-based gradiometers can achieve higher resolutions (e.g. for GOCE, 4mE/rtHz in Earth orbit) considerably better than torsion-balance approaches. However, they are very sensitive to any mismatch between the accelerometers. MEMS technology opens up the possibility of shrinking gravity gradiometers to a portable sensor of several grams. Two miniaturized gradiometers have been developed. Flokstra [7] and coworkers fabricated a MEMS gradiometer with two identical in-plane accelerometers for differential sensing, alleviating the accelerometers' mismatch but suffering from noisy comb capacitive sensing. Ghose and Shea [8] developed a torsion balance based MEMS gradiometer, but optical sensing of the displacement was problematic.

Compared with conventional gradiometers, MEMS gradiometers are relatively larger noise and lower sensitivity since the proof masses have to be smaller and there is limited space for transducers. The way of optimizing these issues without sacrificing miniaturization is to maximize the masses and transducer sensitivity within a certain volume. Proof masses can be increased by bulk micromachining rather than surface microfabrication including attaching extra mass. In terms of displacement transducers, Pike's [9] area-changing capacitive array transducer is a promising solution since it is capable of low noise and high accuracy displacement sensing. To implement such an approach, two sets of capacitive plates are fabricated, one moving set on the proof mass, and the other fixed set on a second bonded die, with the bone thickness setting the capacitance gap. Both the sensing capacitance and displacement output is much larger than the comb-finger geometry for a given die area, though at the cost of introducing a second die. Ideally, the capacitance gap should remain constant to out-of-plane disturbances. Furthermore, compared with Earth's maximum gravity acceleration, the gravity variation range for gradiometers is only 0.7% [10]. Hence, gradiometers require ultra-high sensitivity in a small displacement range. A novel small stroke rotary suspension with very low rotational stiffness for the sensing signal and very high rejection ratios to other vibrations is developed in this paper suitable for use in a torsion-balance-based micromachined gravity gradiometer.

II. DEVICE DESIGN AND MODELLING

The working principal of a gradiometer is that the differential gravitational forces on two proof masses connected at a pivot induce a torque about the pivot that is balanced by a suspension force at a rotation that can be sensed by a periodic-array capacitive displacement transducer. The rotation angle is proportional to the gradient of gravitational field. The three-dimensional schematic of the gradiometer suspension is shown in Fig.1. Four flexural beams with length of L and width w bridge the gap between frame and a central pivot whose radius is r. The two square proof masses with a side length of a are linked at the central pivot. This suspension system supports two suspended masses rotating about the z axis and rejects any unexpected vibrations.

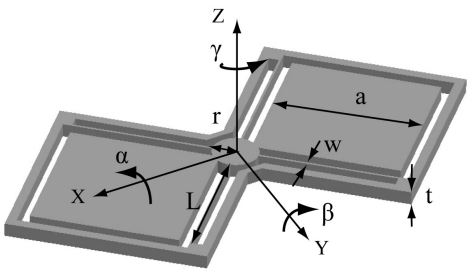

Fig.1. Schematic of the gradiometer suspension

978-1-4799-0162-3/14/$31.00 ©2014 IEEE

To better understand the vibration modes, commercial finite element analysis (FEA) software COMSOL Multi-physics is used to simulate the gradiometer design. Fig.2 illustrates simulation results of first four vibrations modes of gradiometer design in three dimensions. Color distribution in these graphics represents spatial displacements varying from zero (blue) to significant (red). According to the color gradient, the fundamental mode γ is rotating in plane about z axis. The first and third rotational spurious modes β and α are cross-axis rotations about principal y and x axes respectively. Out-of-plane translational vibration is the second spurious mode along z. Apart from these modes, there is another crucial cross-axis mode xy which represents the vertical sag during gravity-gradient sensing.

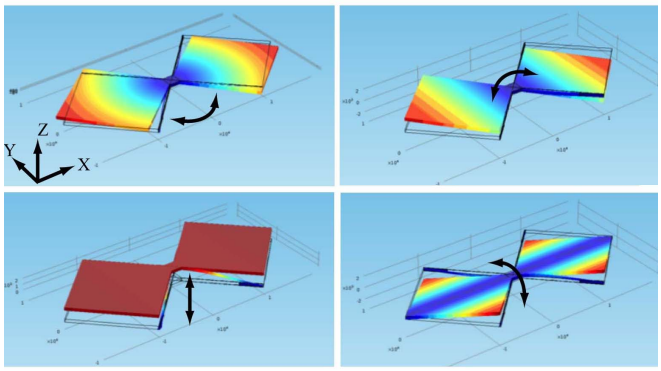

Fig.2. First four vibration modes of the gradiometer in COMSOL

According to stiffness matrix method [11], the stiffness matrix [$\boldsymbol{K}$] can be solved by [$\boldsymbol{K}$] = [$\boldsymbol{F}$] [$\boldsymbol{D}$]$^{-1}$. Here [$\boldsymbol{F}$] and [$\boldsymbol{D}$] are the force matrix and the displacement matrix respectively. Then, the squared angular frequency matrix [$\boldsymbol{\omega^2}$] can be worked out by [$\boldsymbol{K}$] dividing by the inertial matrix [$\boldsymbol{M}$]. Several assumptions are made to simplify the expressions:

- Suspended masses and the pivot are perfectly rigid.
- Suspension beams and pivot are massless.
- Beams deform in the elastic range.
- Beams are very thin, with the beam width w much smaller than its thickness t.
- Pivot radius r is much smaller than beam length L.

The resulting closed-form solutions of the resonant frequencies are listed in Table 1. Further assuming that the ratio of pivot radius to beam length c_{ratio} is small enough to be neglected and the side length of the square mass a is comparable with the spring length L, the rejection ratios of each spurious mode to fundamental mode can be approximately expressed in the last two columns of Table 1. It is clear that all the rejection ratios are inversely proportional to spring width w and the first three rejection ratios are proportional to aspect ratio t/w.

In order to cross check the theoretical formulas derived in Table 1, FEA simulations of the fundamental frequencies were performed with four parameters: beam width w, beam length L, pivot radius r and mass side length a. Comparison results of theory and FEA are plotted in same scales as the variation of the fundamental frequencies to the key design variables are shown in Fig.3. From all the plots, FEA simulation results are

TABLE I. CLOSED-FORM SOLUTIONS OF SUSPENSION ($c_{ratio} = r / L$)

Modes	Expressions	Ratio	Value
$\omega_\gamma^2 = \frac{k_\gamma}{I_{zz}}$	$\frac{8}{7}\frac{E}{\rho}\frac{1}{a^4}\frac{1}{L}w^3(1+3c_{ratio})$	$\frac{f_\gamma}{f_\gamma}$	1
$\omega_\beta^2 = \frac{k_\varphi}{I_{yy}}$	$\frac{2}{3}\frac{E}{\rho}\frac{1}{a^4}\frac{1}{L}wt^2(1-3c_{ratio})$	$\frac{f_\beta}{f_\gamma}$	$0.76\frac{t}{w}$
$\omega_z^2 = \frac{k_z}{m}$	$2\frac{E}{\rho}\frac{1}{a^2}\frac{1}{L^3}wt^2$	$\frac{f_z}{f_\gamma}$	$1.32\frac{t}{w}$
$\omega_\alpha^2 = \frac{k_\varphi}{I_{xx}}$	$4\frac{E}{\rho}\frac{1}{a^4}\frac{1}{L}wt^2(1-3c_{ratio})$	$\frac{f_\alpha}{f_\gamma}$	$1.87\frac{t}{w}$
$\omega_{xy}^2 = \frac{k_{xy}}{m}$	$1\frac{E}{\rho}\frac{1}{a^2}\frac{1}{L}w$	$\frac{f_{xy}}{f_\gamma}$	$0.94\frac{a}{w}$

in good agreement with the closed form solutions. Comparing the results on the same scale it is evident that the fundamental frequency of the gradiometer depends on the beam width and

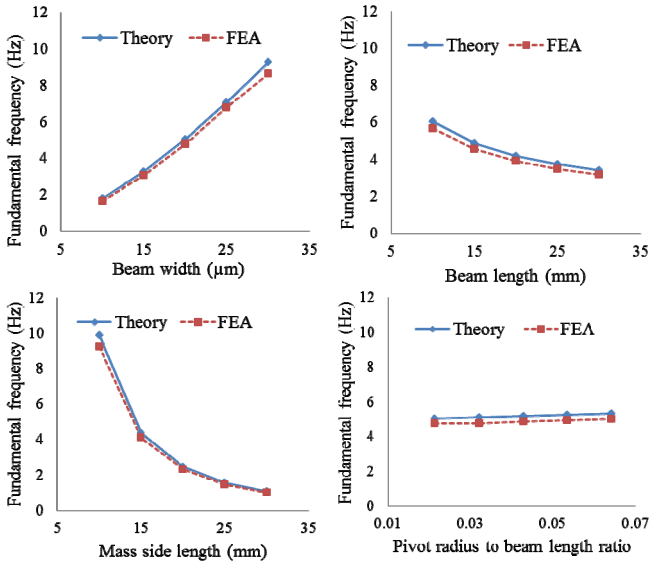

Fig.3. Fundamental frequency with beam width, length, mass side length and the ratios of pivot radius to beam length

mass size rather than beam length and pivot size. Fig.4 illustrates the rejection ratios of the gradiometer's spurious frequencies to its fundamental frequency as a function of the beam width. All FEA simulations agree with the closed-form solutions results, showing that all the rejection ratios go down as beam width increases. With proof mass size of 15 mm and a beam width of 20μm, the first rejection ratio is about 20 and the xy mode rejection ratio reaches around 700. According to all above, it is verified that the derived theoretical formulas are fit for gradiometer suspension system.

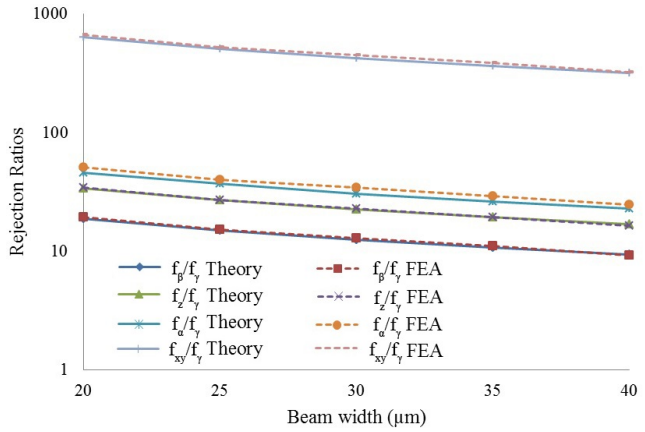

Fig.4. Comparison of theory and FEA results about rejection ratios of spurious frequencies to fundamental frequency

III. EXPERIMENTAL RESULTS

A. Fabrication

In order to verify the dynamic characteristics of gradiometer prototypes, the deep reactive ion etching (DRIE) process was used to fabricate silicon devices for preliminary testing using double-side polished 4-inch silicon wafers with a thickness of 525μm. First, an aluminum layer of 200nm to 400nm was evaporated on the back side of silicon wafer to suppress notching during DRIE through wafer etching. After dehydrated in the oven, the wafer was coated with monolayer primer in a desiccator to improve adhesion between wafer and a thick photoresist layer. Owing to the powerful through DRIE, a 14μm AZ9260 photoresist layer was spin-coated to protect the device regions. After a soft baking and an overnight rehydration, the wafer was exposed in a UV aligner and developed in AZ400K with an O-ring, glass wafer and clips to prevent dissolution of the aluminum backside layer by the developer. After development the DRIE is performed in two steps with a three hour etching without a backing wafer followed by one and a half hours etching with a backing wafer. Finally, the photoresist and aluminum layer are stripped by soaking sample in acetone and AZ400K developer respectively.

The fabricated gradiometer prototype has a proof mass side-length of 15mm, laying down on a one-pound coin for comparison in Fig.5. In order to protect the movable structure from shock, metal-based bumpers are integrated into the proof masses and frames to absorb impact energy. For each bumper set, one hole on the proof mass and two holes on frame are incorporated into the DRIE mask. Then solder balls are loaded into each hole and reflowed. After cooling down, the reflowed solder achieves a specific and consistent profile only depending on the dimensions of silicon holes. For this design, the protrusions from each solder hole restrict masses motion in the range of ±125μm corresponding to ±0.3° rotation. For such a range the relation between the rotation angle and applied torque is linear. When a large acceleration is applied to the gradiometer, the two solder cylinders will absorb impact energy by plastic deformation protecting the movable structure.

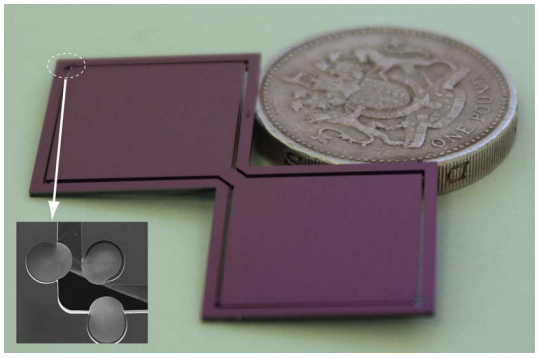

Fig.5. Fabricated gradiometer on one British pound coin and reflowed solder cylinders as bumpers

B. Measurement results

The vibration frequencies of gradiometer were measured in SEM based on Pike's dynamic determination method [12]. In SEM, the electro-beam raster is parallel to the vibration direction; therefore, the position of the oscillating suspension is captured by each line scan. In this case, the period of oscillation can be derived by total oscillation time dividing by oscillation count yielding the oscillation frequency, shown in (1):

$$f_{osc} = \frac{L_{frame}}{L_{osc}} \cdot \frac{N_{osc}}{t_{frame}} = \frac{1.327mm \times 24}{741.5\mu m \times 12.7s} = 3.38Hz \quad (1)$$

Here L_{frame} and t_{frame} are the height and period of a whole SEM scan; N_{osc} and L_{osc} are oscillation numbers and its height in a certain area of interest. Hence, the measured prototype in Fig. 6 gives its fundamental frequency of 3.38Hz.

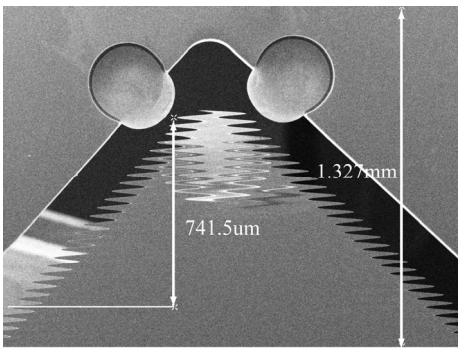

Fig.6. Determination of fundamental frequency by SEM.

Once the gradiometer is excited in the high vacuum of the SEM chamber, it oscillates at both the fundamental mode and also higher-order spurious modes and these can be observed by tilting to the appropriate geometry. The first and third spurious modes are cross-axis rotational modes about the two in-plane principal axes of gradiometer. Hence, the most evident positions for visualizing the vibration are the corners of the proof masses. However, as there are bumpers prevent direct observation of these modes. The out-of-plane vibration can be observed by tilting to nearly vertical with the spring beam parallel to the slow-scan direction of the SEM. As shown in Fig.7, the natural vibration is overlapped by out-of-plane

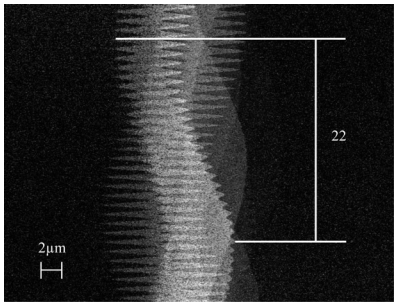

Fig.7. Determination of fundamental frequency by SEM.

oscillation with higher frequency. In half a period of fundamental oscillation, 22 out-of-plane oscillations are visible, giving a second-mode rejection ratio of 44. The corresponding out-of-plane frequency is calculated according to measured fundamental frequency and their ratio and the results of theory, FEA and observation are compared in Table 2.

TABLE II. RESULTS COMPARISON

	Theory	**FEA**	**Measurement**
f_γ (Hz)	3.62	3.38	3.38
f_β (Hz)	85.07	77.06	-
f_z (Hz)	147.7	145	148.72
f_α (Hz)	209.2	208.88	-
f_{xy} (Hz)	3002	2701.6	-
f_β / f_γ	23.5	22.8	-
f_z / f_γ	40.8	42.9	44
f_α / f_γ	57.8	61.8	-
f_{xy} / f_γ	829.4	799.3	-

IV. DISCUSSION

The FEA results are slightly below the closed-form results and the divergences become larger as the fundamental frequency increases. This can be attributed to the out-of-plane moment of inertia I_{zz} for proof masses neglecting the pivot size. Due to the much smaller pivot radius compared with beam length, the almost constant relative deviation between FEA and theory can generally be ignored.

With the constant wafer thickness and proof-mass size, thinner spring beams give improved spurious-mode rejection. For the most important first-spurious-mode rejection ratio, the maximum value is 76% of the beam depth-to-width aspect ratio with an upper value given by the limitations of the DRIE process. The suspension optimization can be simplified to the design rule that decreasing the beam width reduces the fundamental frequency and improves the rejection ratios.

In practical applications, the gradiometer generally experiences the rotation by angular acceleration which is even larger than the gravity gradient signal. Therefore, in order to decouple acceleration noise from gradient sensing, the gradiometer system has to work in differential mode. In the prototype design, two identical sensors are bonded back to back with the angle difference of 90°. In this case, the subtraction of outputs from two sensors is the doubled gravity gradient induced rotation signal. However, the summation of outputs is the doubled acceleration induced rotation. Hence, apart from precise gradient sensing, the gradiometer system is promising to be a high performance gyroscope but the dynamic range is limited to its actuator performance.

V. CONCLUSION

In this paper, a rotary suspension system for torsion balanced gravity gradiometer is presented. Both FEA modelling and measurement results agree with the closed form formulas for each dynamic mode. The rejection ratios of the spurious-mode to fundamental frequencies can be quickly estimated by the suspension beam aspect ratio, and will be limited by the processing techniques used. The microfabricated gravity gradiometer prototype gives a fundamental frequency of 3.38Hz with the calculated first rejection ratio of around 23.

ACKNOWLEDGMENT

We would like to thank Prof. Andrew Holmes for valuable discussions and Dr. M. Ahmad, Dr. A. K. Delahunty and Dr. A. Mukherjee for fabrication suggestions.

REFERENCES

[1] D. DiFrancesco, A. Grierson, D. Kaputa, and T. Meyer, "Gravity gradiometer systems-advances and chanllenges," Geophysical Prospecting, 2009, vol. 57, pp. 615-623

[2] J. A. Richeson, "Gravity gradiometer aided inertial navigation within non-GNSS environments," University of Maryland PhD Thesis, 2008

[3] C. A. Murphy, "The Air-FTG airborne gravity gradiometer system," ASEG-PESA Airborne Gravity 2004 Workshop, Sydney, 2004, pp.7-14

[4] M. H. Dransfield and J. B. Lee, "The FALCON airborne gravity gradiometer survey systems," ASEG-PESA Airborne Gravity 2004 Workshop, Sydney, 2004, pp.15-19

[5] B. Tapley, et al., "GGM02-An improved earth gravity field model from GRACE," Journal of Geodesy, 2005, vol. 79, pp.467-478

[6] R. Rummel, W. Y. Yi, and C. Stummer, "GOCE gravitational gradiometer," Journal of Geodesy, 2011, vol. 85, pp.777-790

[7] J. Flokstra, R. Cuperus, R. J. Wiegerink, and M. C. van Essen "A MEMS-based gravity gradiometer for future planetary missions," Cryogenics, 2009, vol. 49, pp.665-668

[8] K. Ghose and H. R. Shea, "Fabrication and testing of a MEMS based Earth sensor," IEEE Transducers 2009, Denver, 2009, pp.327-330

[9] W. T. Pike, et al., "Design, fabrication and testing of a micromachined seismometer with NANO-G resolution", IEEE Transducers 2009, Denver, 2009, pp.668-671

[10] C . Hirt, S. Claessens, T. Fecher, M. Kuhn, and R. Pail, "New ultrahigh-resolution picture of Earth's gravity field," Geophysical research letters, 2013, vol. 40, pp.4279-4283

[11] C. L. Dym, "Structural modelling and analysis," Cambridge University Press, 2005

[12] W. T. Pike and I. M. Standley, "Determination of the dynamics of micromachined lateral suspensions in the scanning electron microscope," Journal of Micromechnics and Microengineering, 2005, vol. 15, pp. S82-S88